Particle Deposition Driven by Evaporation in Membrane Pores and Droplets

Dominic Jeong, Juliet Jiang, Ruohan Zhang [†]

Faculty project advisor: Thomas Witelski[‡], Graduate Student project manager: Yuqing Dai[§]

Abstract. This paper investigates particle deposition driven by fluid evaporation in a single pore channel representative of those found in porous membranes. A moving boundary problem for the 2D heat equation is coupled with an evolution equation for the pore radius, and describes the physical processes of fluid evaporation, diffusion of the particle concentration, and deposition on the pore channel wall. Furthermore, a stochastic differential equation (SDE) approach based on a Brownian motion particle-level description of diffusion is used as a similar phenomenological representation to the partial differential equation (PDE) model. Sensitivity analysis reveals trends in dominant model parameters such as evaporation rate, deposition rate, the volume scaling coefficient, and investigates the monotonicity of concentration. Evaluations of the asymptotically reduced model and the SDE model against the 2D PDE model are done in terms of the pore radius and solute concentration over time. For further exploration, we apply the model to a 2D droplet as well with both deterministic and stochastic approaches.

Key words. diffusion, evaporation, particle deposition, stochastic differential equations, partial differential equations, moving boundary problem

1. Introduction.

When fluid in an open container evaporates, any non-volatile impurities will eventually deposit as residue on the walls of the container. Evaporation of the solvent increases particle concentration until a saturation point is reached, where particles then exit the solution and adhere to the internal walls. The process leaves a distribution of particle mass on dried portions of the container. This phenomenon exists in porous media, which can be described as numerous layers of thin filter membranes composed of microscopic pores, where invasion of a volatile liquid occurs. The evaporation of the impure fluid leads to accumulation of deposited particles such as dirt and dust inside the pore structure. The accumulation of these particles has the potential to cause clogging within the pores, leading to contamination and overall degradation of the material. The problem is well worth investigating as different types of porous media appear in deep filtration and fluid transport problems, occurring naturally from extracellular space to industrial material structure [2, 6]. Pore structure, transport processes, and contaminant deposition all influence the solvent evaporation rate [14]. Thus, given the interplay of these processes, understanding the behavior and patterns of particle deposition and solvent evaporation can provide helpful information for industrial and medical fields to limit contamination and prevent clogging through improved material design.

Existing models have investigated the evaporation process from different perspectives and fields, including factors such as medium properties, internal transport processes, pore geometry, and pore wettability [8, 10]. For this article, the model presented follows along the lines of those presented in a series of annual workshops on Mathematical Problems in Industry

[†]Department of Mathematics, Duke University (dominic.jeong@duke.edu, juliet.jiang@duke.edu, ruohan.zhang690@duke.edu)

[‡]Department of Mathematics, Duke University (witelski@math.duke.edu)

[§]Department of Mathematics, Duke University (ydai39@math.duke.edu)

(MPI) in 2020 and 2021, where several industrial representatives from W. L. Gore & Associates presented the problem of contamination in porous media or filters. In their work, researchers developed a model that describes evaporation and deposition in a single cylindrical pore structure [1], examined the effect of physical parameters such as pore length and fluid wetting properties, and observed the response of particle mass distribution to cycles of wetting and drying [14]. This paper makes use of similar important physical phenomena such as evaporation, deposition, and key model attributes (pore radius, fluid concentration).

However, the MPI solutions require a limiting case where pores have small aspect ratios (i.e. they are long and narrow). This study considers the model for two-dimensional (2D) domains (with finite aspect ratios) with two moving boundaries, eliminating those geometric assumptions. Additionally, finite difference methods used on irregular boundaries can have lower accuracy due to limited spatial resolution, causing mass to leak from the system. To prevent the loss of mass, rather than having irregular domains shrink as boundaries move, we instead implement fixed computational domains through a change of variables. Moreover, this paper uses stochastic differential equations (SDEs) to model particle behavior in the bulk through tracking individual particle trajectories rather than the fluid body as a whole. The use of SDEs requires the formulation of boundary conditions at the edges of the pore channel and at the fluid-air interface. SDE boundary conditions are still being studied or are very complicated [9], so we are interested in creating SDE boundary conditions that are simpler and easier to manipulate. If the SDE and PDE models show phenomenological similarity, we will have shown the two approaches can describe evaporation and deposition processes in a micro-scale pore.

Other scenarios possessing evaporation-deposition interactions include the case where fluid no longer spans the entirety of an open pore channel after evaporation. Surface tension causes the remaining fluid to adhere to side walls as droplets. Droplets along a pore channel are analogous to liquid spills leaving particle-laden drops on a horizontal surface. Further evaporation of fluid in these cases typically results in particles dispersing and leaving unique deposition patterns around the perimeter of the droplet or spill. The mechanism behind development of these ring-like deposits is commonly attributed to the coffee ring effect, and the phenomenon can be detrimental in materials that require uniform deposition [16]. It has been shown that the coffee ring effect originates from outward capillary flow and the droplet's surface tension [7]. However, even without these conditions, understanding deposition patterns through constructing mathematical models can be helpful for many applications. Thus, to conduct a more comprehensive study of particle evaporation and deposition behavior, it is also important to investigate how these droplets evolve.

The outline of this paper begins with the construction of the 2D PDE model, detailed from solving the dimensional problem to constructing the non-dimensional model on the computational domain. The subsequent section describes the SDE model with a proposed stochastic algorithm and boundary conditions. Next, an asymptotically reduced 1D model is derived from the 2D model. Results are presented by visual comparison and numerical metrics such as mass and pore radius or concentration evolution, and are followed by a systematic summary of parameter analyses. Lastly, we apply similar computational methods and PDE vs. SDE comparisons to a model of an evaporating droplet.

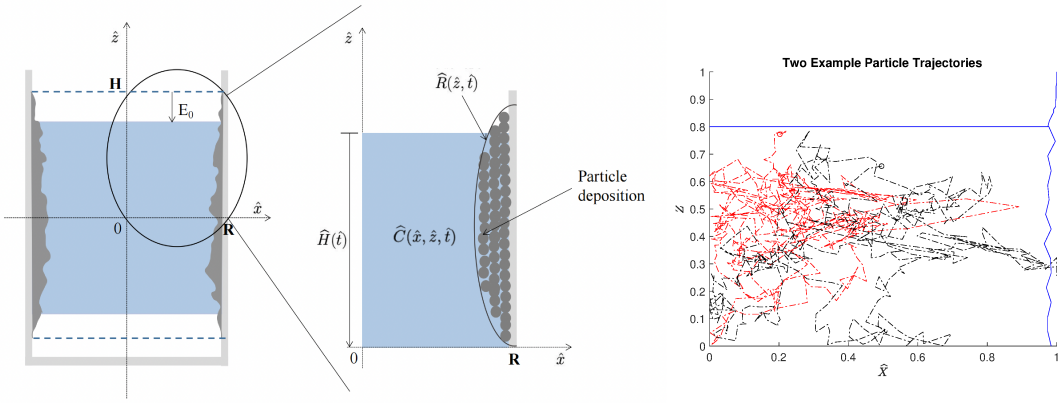

Figure 1: **Left**: Schematic of the reduction from the physical pore to the 2D quarter section described in the PDE model. $\boldsymbol{H}$ and $\boldsymbol{R}$ describe the initial state of the physical pore channel, whereas $\widehat{R}(\hat{z},\hat{t})$ and $\widehat{H}(\hat{t})$ represent the evolving dimensions of the pore in the mathematical model. $\widehat{C}(\hat{x},\hat{z},\hat{t})$ describes concentration in the particle-laden fluid, and E_0, the evaporation rate, lowers the fluid height. Circular particles illustrate mass accumulation along the right wall. **Right**: Two example particle trajectories in the fluid of the SDE model. Particles move randomly and are contained in the fluid. If adsorption occurs at the wall, accumulation causes the pore radius to narrow.

2. Model Formulation.

In this section, investigation of the reduced 2D model for a single pore filled with fluid is conducted. As shown in Figure 1 (left), the rectangular pore is sectioned into symmetrical quarters from the horizontal and vertical center. In the vertical direction, evaporation takes place at the upper and lower fluid-air interfaces. As evaporation occurs, fluid height decreases and particles in the fluid, represented in Figure 1 (left) in gray, are continuously deposited along the internal pore surface in the wet portions of the channel. In the dry portions of the pore, particles remain on the wall, forming a fixed distribution mass as the interface lowers. In the horizontal direction, the radius of the pore channel narrows over time due to particle accumulation on the internal wall. Therefore, the presented problem consists of two types of moving boundaries: the uniform air-fluid evaporation interface and the nonuniform, shrinking radius for the fluid-solid deposition interface. Instead of the physical meniscus shape, we assume the fluid-air interface to be flat and independent of the horizontal position $\hat{x}$. The fluid-air interface lowers according to a constant evaporation rate, denoted by E_0.

Figure 1 (left) also shows that the model in this paper only examines the top-right section of the channel. The complete behavior of the rectangular pore with suspended liquid can be inferred from the quarter section. Gravity is neglected in the model to achieve this vertical symmetry between the upper and lower part of the fluid. The 2D diffusion equation is used to model the concentration of particles in the fluid body, and is coupled with a PDE describing the radius of the pore channel. The solvent evaporation rate, particle deposition rate, fluid initial concentration, and the diffusion of the concentration all contribute to the shape of the

accumulating wall, and thus we closely investigate the effect of these properties in our model.

Furthermore, since the random motion of particles in the fluid is given by Brownian motion, it is of interest to see how an SDE model may perform alongside the PDE model, further described in section 3. Concentration can likewise be defined as a probability density function of individual particle trajectories [11]. By computationally tracking each particle trajectory over time as shown in Figure 1 (right), the SDE model defines concentration as the proportion of particles present in a given area to determine levels of saturation at the pore wall, from which the probability of local deposition is evaluated. The SDE model gives a micro-particle approach rather than illustrating macroscopic behavior. However, it is expected to demonstrate a good agreement of behavior with the PDE model.

The initial pore radius is denoted as $\boldsymbol{R}$, and the initial height of the fluid surface to the vertical center of the pore is $\boldsymbol{H}$ as shown in Figure 1 (left). This model assumes the dilute case; therefore, the pore channel is initially completely filled with fluid of low particle concentration. The particle concentration is also uniform across the entire fluid body. Adsorption will occur on the wall of the channel when local concentration near the boundary exceeds the saturation concentration defined in the model. The adsorption process is also irreversible, meaning once the particles deposit onto the wall, they do not re-enter the fluid. For computational purposes, we ignore the thermodynamic effects to the model including the effect of phase changes, temperature variations, or humidity variations. Lastly, we also neglect the net drift velocity of particles in the fluid.

2.1. 2D PDE problem. As shown in Figure 1, a single 2D pore channel is sectioned with $\hat{z} = 0$ and $\hat{x} = 0$ being planes of symmetry horizontally and vertically. A system of partial differential equations is used to model the quarter section of the pore where $\hat{z} \geq 0$ and $\hat{x} \geq 0$, and $\hat{t}$ as the time variable. With the assumptions above and for $\hat{t} \geq 0$, $\widehat{H}(\hat{t})$ is used to denote the height of the top flat surface from the axis $\hat{x} = 0$. The radius of the pore is represented by

$$\widehat{R}_{full}(\hat{z}, \hat{t}) = \begin{cases} \widehat{R}_{dry}(\hat{z}) & \widehat{H}(\hat{t}) < \hat{z} \leq \boldsymbol{H}, \\ \widehat{R}_{wet}(\hat{z}, \hat{t}) & 0 \leq \hat{z} \leq \widehat{H}(\hat{t}). \end{cases} \tag{2.1}$$

The region $\widehat{H}(\hat{t}) < \hat{z} \leq \boldsymbol{H}$, above the fluid, is considered as the 'dry' region where the radius does not further evolve, and we define $\widehat{R}_{dry}(\widehat{H}(\hat{t})) := \widehat{R}_{wet}(\widehat{H}(\hat{t}), \hat{t})$ at each time by continuity at the interface. For the rest of the paper, the model will focus on $\widehat{R}_{wet}(\hat{z}, \hat{t})$, simply referred to as $\widehat{R}(\hat{z}, \hat{t})$. To denote the fluid concentration, we use

$$\widehat{C}(\hat{x}, \hat{z}, \hat{t}) \quad \text{defined on the evolving domain} \quad \begin{cases} 0 \leq \hat{x} \leq \widehat{R}(\hat{z}, \hat{t}), \\ 0 \leq \hat{z} \leq \widehat{H}(\hat{t}). \end{cases} \tag{2.2}$$

The particle concentration in the pore channel is modeled by the diffusion equation, given by

$$\frac{\partial \widehat{C}}{\partial \hat{t}} = D \left(\frac{\partial^2 \widehat{C}}{\partial \hat{x}^2} + \frac{\partial^2 \widehat{C}}{\partial \hat{z}^2} \right), \tag{2.3}$$

where D is the diffusion constant. Since the model works upon a quarter section of the entire pore channel, the left and bottom boundaries are the planes of symmetry of the fluid body.

Thus, they are treated as reflecting boundaries, or Neumann symmetry boundary conditions, written as

$$\left.\frac{\partial \widehat{C}}{\partial \hat{z}}\right|_{\hat{z}=0} = 0, \qquad \left.\frac{\partial \widehat{C}}{\partial \hat{x}}\right|_{\hat{x}=0} = 0. \tag{2.4}$$

The height of the fluid decreases due to evaporation, rendering the top surface, $\hat{z} = \widehat{H}$, a moving boundary. The decreasing height is determined by the constant evaporation rate

$$\frac{d\widehat{H}}{d\hat{t}} = -E_0, \tag{2.5}$$

and the corresponding no-flux condition at the moving boundary is

$$\left(-\widehat{C}\frac{\partial \widehat{H}}{\partial \hat{t}} - D\frac{\partial \widehat{C}}{\partial \hat{z}}\right)\Bigg|_{\hat{z}=\widehat{H}(\hat{t})} = 0. \tag{2.6}$$

Additionally, while fluid evaporates, deposition occurs when local concentration near the wall exceeds a defined saturation concentration C_{sat}. The resulting precipitation flux is defined by $\widehat{Q}(\widehat{C})$ where

$$\widehat{Q}(\widehat{C}) = \lambda \max(\widehat{C} - C_{sat}, 0), \tag{2.7}$$

with $\lambda > 0$ as a dimensional deposition rate. Since deposition happens gradually at the right wall as time goes by, this side wall is also a moving boundary and could be represented by the surface $\hat{x} = \widehat{R}(\hat{z}, \hat{t})$. The moving boundary condition describing a narrowing pore radius is then represented through a Robin boundary condition as

$$\left(-\widehat{C}\frac{\partial \widehat{R}}{\partial \hat{t}} - D\frac{\partial \widehat{C}}{\partial \hat{x}} + D\frac{\partial \widehat{C}}{\partial \hat{z}}\frac{\partial \widehat{R}}{\partial \hat{z}} - \widehat{Q}(\widehat{C})\sqrt{1+\widehat{R}_{\hat{z}}^2}\right)\Bigg|_{\hat{x}=\widehat{R}(\hat{z},\hat{t})} = 0, \tag{2.8}$$

where the right boundary condition contains a flux term built upon $\widehat{Q}(\widehat{C})$. Flux exiting the fluid body yields particles accumulating on the wall and narrowing the pore radius. Thus, the inward-moving wall can be described as

$$\frac{\partial \widehat{R}}{\partial \hat{t}} = -\chi \widehat{Q}(\widehat{C})\sqrt{1+\widehat{R}_{\hat{z}}^2}, \quad \hat{z} \in [0, \widehat{H}(\hat{t})], \tag{2.9}$$

where $\chi > 0$ is a dimensional volume scaling coefficient [14]. We use χ to describe the compression of particles when exiting the solvent and adhering to the wall.

To derive the boundary conditions for Equations (2.6) and (2.8), we apply the Leibniz integral rule to a general expression for the rate of change of mass. The derivation is detailed in Appendix A. Equation (A.5), a general moving boundary condition with flux, is applied to: (i) the surface $\hat{x} = \widehat{R}(\hat{z}, \hat{t})$ at the wall with prescribed flux of particles Q and (ii) the evaporating surface $\hat{z} = \widehat{H}(\hat{t})$ with no flux to obtain the two Robin boundary conditions in

Table 1: Table of Dimensional Parameters. Values displayed comprise an example set of parameters taken from [14]. The volume scaling coefficient is set to 0.8 as a conversion factor between fluid concentration and the corresponding deposited volumes on the pore wall, and the saturation concentration is chosen as 0.5 M as per [4]. These values may represent generic reference scales that are physically plausible, or re-scaled through non-dimensionalization, as discussed in Section 2.1.1.

Parameter	**Symbol**	**Value**
Evaporation rate (mm/h)	E_0	0.5
Diffusion rate (mm^2/h)	D	1
Precipitation rate coefficient (mm/h)	λ	1
Volume scaling coefficient	χ	0.8
Saturation concentration (mol/L)	C_{sat}	0.5

this section. Additionally, the initial conditions at $\hat{t} = 0$ of the system of PDE describing the pore channel is denoted as

(2.10)
$$\widehat{H}(0) = \boldsymbol{H}, \qquad \widehat{R}(\hat{z}, 0) = \boldsymbol{R} \quad \text{on } 0 \le \hat{z} \le \boldsymbol{H}, \qquad \widehat{C}(\hat{x}, \hat{z}, 0) = \boldsymbol{C_0} \quad \text{on } \begin{cases} 0 \le \hat{x} \le \boldsymbol{R}, \\ 0 \le \hat{z} \le \boldsymbol{H}. \end{cases}$$

Example choices of the constant parameters used in the PDE system are defined in Table 1. With the above initial condition, (2.5) can be solved to give the height as

(2.11)
$$\widehat{H}(\hat{t}) = \boldsymbol{H} - E_0 \hat{t}.$$

Then the ultimate ending time equals $\hat{t}_{end} = \boldsymbol{H}/E_0$, where $\widehat{H}(\hat{t}_{end}) = 0$ and the model stops as the fluid is completely evaporated. However, the model assumes dilute regimes and the concentration $\widehat{C}$ diverges to infinity as time approaches $\hat{t}_{end}$ and as the solvent evaporates. Thus, we will stop simulations before reaching $\hat{t}_{end}$, before the concentration becomes too high.

2.1.1. Non-dimensionalization. In order to have a better understanding of the model's intrinsic behavior, non-dimensionalization is applied to the 2D model with equations (2.3)-(2.8) so the influence of parameters does not depend on dimensional values. The results in this section are also implemented in the droplet model discussed in a further section. To conduct non-dimensionalization, the variables are re-scaled such that

$$\tilde{x} = \hat{x}/\boldsymbol{R}, \quad \hat{x} \in [0, \widehat{R}(\hat{z}, \hat{t})] \qquad \tilde{z} = \hat{z}/\boldsymbol{H}, \quad \hat{z} \in [0, \widehat{H}(\hat{t})].$$

For further convenience, the timescale T is chosen to be dependent on the rate of diffusion and the length of the pore: $T = \boldsymbol{H}^2/D$. Thus, $\hat{t}$ is re-scaled as

$$\tilde{t} = \hat{t}/T.$$

Table 2: Table of Non-dimensional Parameters

Description	Symbol	Value
Aspect ratio	ϵ	$\frac{\boldsymbol{R}}{\boldsymbol{H}}$
Peclet number (evaporation rate)	β	$\frac{E_0 \boldsymbol{H}}{D}$
Damkohler number (deposition rate)	ω	$\frac{\lambda \boldsymbol{H}^2}{D\boldsymbol{R}}$
Volume scaling fraction	γ	χC_{sat}
Initial concentration scaling	ρ	$\boldsymbol{C_0}/C_{sat}$

These re-scales are then applied to concentration, radius, and precipitation flux function of the model, generating

$$\widehat{C}(\hat{x},\hat{z},\hat{t}) = C_{sat}\tilde{C}(\tilde{x},\tilde{z},\tilde{t}), \qquad \widehat{R}(\hat{z},\hat{t}) = \boldsymbol{R}\tilde{R}(\tilde{z},\tilde{t}), \qquad \widehat{Q}(\widehat{C}) = \lambda C_{sat}\tilde{Q}(\tilde{C}),$$

where now the precipitation flux is $\tilde{Q}(\tilde{C}) = \max(\tilde{C}-1, 0)$. These scaled variables and functions replace the dimensional counterparts in the previous equations. The dimensionless height (2.11) is then

$$\tilde{H}(\tilde{t}) = 1 - \beta\tilde{t}, \tag{2.12}$$

where the Péclet number β is adopted to describe the evaporation rate. Furthermore, other dimensional constants are replaced with non-dimensional parameters, where a summary of all dimensionless parameters is listed in Table 2. For example, aspect ratio $\epsilon = \boldsymbol{R}/\boldsymbol{H}$ is used to define the geometry of the pore, and if the pore is long and narrow, ϵ approaches zero. That is, the original diffusion equation and boundary conditions are first scaled with the scaled coefficients, and then the non-dimensional parameters are substituted. The 2D diffusion equation (2.3) becomes

$$\epsilon^2\tilde{C}_{\tilde{t}} = \tilde{C}_{\tilde{x}\tilde{x}} + \epsilon^2\tilde{C}_{\tilde{z}\tilde{z}}. \tag{2.13}$$

The boundary conditions at the bottom and left reflecting surfaces (2.4) remain

$$\tilde{C}_{\tilde{z}} = 0 \qquad \tilde{C}_{\tilde{x}} = 0. \tag{2.14}$$

The boundary condition for the top surface (2.6) transforms to

$$\beta\tilde{C} - \tilde{C}_{\tilde{z}} = 0, \tag{2.15}$$

The right boundary condition with flux due to deposition (2.8) is calculated as

$$\epsilon^2(\tilde{C}_{\tilde{z}}\tilde{R}_{\tilde{z}} - \tilde{C}\tilde{R}_{\tilde{t}}) - \tilde{C}_{\tilde{x}} = \omega\epsilon^2\tilde{Q}(\tilde{C})\sqrt{1+\epsilon^2(\tilde{R}_{\tilde{z}})^2} \tag{2.16}$$

with ω acting as a deposition rate. The rescaled equation for the evolution of the wall (2.9) is now

$$\epsilon^2 \tilde{R}_{\tilde{t}} = -\omega\gamma\epsilon^2 \tilde{Q}(\tilde{C})\sqrt{1+\epsilon^2(\tilde{R}_{\tilde{z}})^2} \tag{2.17}$$

with γ incorporated as the non-dimensional volume scaling coefficient. The initial conditions for the non-dimensional model becomes

$$\widetilde{C}(\tilde{x},\tilde{z},0)=\rho, \qquad \widetilde{R}(\tilde{z},0)=1, \qquad \widetilde{H}(0)=1. \tag{2.18}$$

In the next section, we execute a change of variables to simplify numerical computation. The motivation behind having this nondimensionalized and non-computationally modified version of the system as an intermediate step is to use it for asymptotically reducing the model which is described later in the paper.

2.1.2. Computational Method. To produce an accurate study of the particle concentration in the irregular domain due to the nonuniform pore wall, a numerical approach of transforming the physical domain onto a fixed computational domain is applied. This transformation is necessary because finite difference methods provide limited spatial resolution, which cannot fully capture the irregular shape of the boundary over time. Without computational scaling, finite difference methods would introduce errors when calculating flux and when applying boundary conditions, often causing the system to lose mass. Therefore, the moving boundary problem is mapped onto fixed computational domains in both the $\tilde{x}$ and $\tilde{z}$ direction. This is done by scaling

$$x=\frac{\tilde{x}}{\widetilde{R}(\tilde{z},\tilde{t})}, \quad z=\frac{\tilde{z}}{\widetilde{H}(\tilde{t})}, \quad t=\tilde{t},$$

such that $x\in[0,1]$ and $z\in[0,1]$. To define $C(x,z,t)$ and $R(z,t)$, we apply the following change of variables,

$$\widetilde{C}(\tilde{x},\tilde{z},\tilde{t})=C\left(\frac{\tilde{x}}{\widetilde{R}(\tilde{z},\tilde{t})},\frac{\tilde{z}}{\widetilde{H}(\tilde{t})},\tilde{t}\right), \quad \widetilde{R}(\tilde{z},\tilde{t}\,)=R\left(\frac{\tilde{z}}{\widetilde{H}(\tilde{t})},\tilde{t}\right). \tag{2.19}$$

Substituting the scaled variables x and z and the scaled functions C and R into the system of non-dimensionalized PDEs describing the simplified 2D pore channel problem, Equation (2.13) simulating the main fluid body becomes

$$\begin{aligned}\epsilon^2\left(C_t+\frac{z\beta}{H}C_z+\left(\frac{x}{R}\frac{z\beta R_z}{H}-\frac{xR_t}{R}-\frac{2xR_z^2}{R^2H^2}+\frac{xR_{zz}}{RH^2}\right)C_x\right)=\\ \frac{1}{R^2}C_{xx}+\epsilon^2\left(-\frac{2xR_z}{RH^2}C_{xz}+\left(\frac{xR_z}{RH}\right)^2C_{xx}+\frac{1}{H^2}C_{zz}\right).\end{aligned} \tag{2.20}$$

The new equation holds on the computational domain $[0,1]\times[0,1]$ and the four boundary conditions are then transformed into

$$\left[\epsilon^2\left\{-C\left(R_t-\frac{zR_z}{H^2}\right)+\frac{R_z}{H}\left(\frac{C_z}{H}-\frac{C_xR_z}{R^2H}\right)\right\}-\frac{C_x}{R}\right]_{x=1}=\omega\epsilon^2Q(C)\sqrt{1+\epsilon^2\frac{1}{H^2}R_z^2}, \tag{2.21}$$

$$\left[C\beta-\frac{C_z}{H}\right]_{z=1}=0, \qquad \frac{1}{R}C_x\Big|_{x=0}=0, \qquad \frac{1}{H}C_z\Big|_{z=0}=0, \tag{2.22}$$

and the deposition equation that describes the evolution of the wall geometry

$$\epsilon^2\left(R_t - \frac{\beta z}{H^2}R_z\right) = -\omega\gamma\epsilon^2 Q(C)\sqrt{1+\frac{\epsilon^2 R_z^2}{H^2}}. \tag{2.23}$$

The system of non-dimensionalized PDEs on the computational domain is solved in MATLAB, making use of the forward Euler method in time with an upwind scheme for Equation (2.23) and a centered finite difference method in space for Equation (2.20). One-sided derivatives were used for boundary conditions. Table 1 summarizes parameters like evaporation rate, precipitation rate, and other initial conditions used in the model and gives example values used in determining a computational solution. We may also use a range of values for each parameter that we use to systematically analyze the model's behavior.

3. SDE problem. A stochastic representation for the particle concentration will allow for simulations of individual particle trajectories and a particle-level understanding of the model. In higher dimensions, SDEs can be less computationally demanding than finite difference methods for PDEs and can operate on parallel machines [9]. Diffusion of particle concentration is inherently stochastic and is described by Brownian motion [11]. Equation (2.3) models 2D isotropic diffusion and can be expressed in terms of the SDEs

$$d\widehat{X}_t = \hat{\sigma}_x dW_t \qquad d\widehat{Z}_t = \hat{\sigma}_z dW_t. \tag{3.1}$$

Here, a standard Wiener process (i.e. Brownian motion) is comprised of $dW_t \sim \mathcal{N}(0, \Delta t)$ and $\hat{\sigma}$ is found from the diffusion constant D with the relationship $\hat{\sigma}_x = \hat{\sigma}_z = \sqrt{2D}$. However, in the nondimensionalized diffusion equation, Equation (2.13), the diffusion coefficient is re-scaled in the $\widetilde{X}$ and $\widetilde{Z}$ directions, and is dependent on the parameter ϵ. Values for $\tilde{\sigma}_x$ and $\tilde{\sigma}_z$ are $\sqrt{2}/\epsilon$ and $\sqrt{2}$, respectively.

In the computational version of the problem, additional drift terms μ are generated and diffusion σ in the x and z directions also become interdependent. Written in vector form, the resultant stochastic process becomes

$$d\vec{X}_t = \vec{\mu}(\vec{X}_t, t)dt + \boldsymbol{\sigma}(\vec{X}_t, t)d\vec{W}_t, \tag{3.2}$$

where $\vec{\mu}$ is the drift vector, $\vec{X}_t = (X_t, Z_t)$, and $\boldsymbol{\sigma}$ is a 2 by 2 matrix found from the diffusion tensor $D = \frac{1}{2}\boldsymbol{\sigma}\boldsymbol{\sigma}^\top$. The density function for the distribution of $\vec{X}_t$ is governed by the Fokker-Planck (FP) equation [11]. In 2D, the FP equation for $C(x, z, t)$ is

$$\frac{\partial C}{\partial t} + \frac{\partial}{\partial x}(\mu_x C) + \frac{\partial}{\partial z}(\mu_z C) = \frac{\partial^2}{\partial x^2}(D_{xx}(x,z,t)C) + 2\frac{\partial^2}{\partial z \partial x}(D_{xz}(x,z,t)C) + \frac{\partial^2}{\partial z^2}(D_{zz}(x,z,t)C), \tag{3.3}$$

which comes in similar form as our 2D diffusion equation (2.20) in the computational domain:

$$C_t + \left(\frac{x}{R}\frac{z\beta R_z}{H} - \frac{xR_t}{R} - \frac{2xR_z^2}{R^2H^2} + \frac{xR_{zz}}{RH^2}\right)C_x + \frac{z\beta}{H}C_z = \left(\frac{1}{\epsilon^2 R^2} + \left(\frac{xR_z}{RH}\right)^2\right)C_{xx} - \frac{2xR_z}{RH^2}C_{xz} + \frac{1}{H^2}C_{zz}. \tag{3.4}$$

We proceed with matching terms between Equations (3.3) and (3.4) (i.e. time derivatives term, diffusive terms with second partials, advective terms with first partials) to obtain forms for the drift and diffusion coefficients, $\mu(x,z,t)$ and $\boldsymbol{\sigma}(x,z,t)$. Then, application of these coefficients to Equation (3.2) gives an SDE representation of the 2D scaled model.

Discretization of the SDE model relies on the Euler-Maruyama method, commonly used to simulate SDEs. The numerical approximation of Equation (3.2) becomes $\vec{X}_{t+\Delta t} - \vec{X}_t = \vec{\mu}(\vec{X}_t, t)\Delta t + \boldsymbol{\sigma}\Delta\vec{W}_t$. If we let $\zeta_i := \frac{1}{\sqrt{\Delta t}}\Delta W_{i,t} \sim \mathcal{N}(0,1)$, the step equations that govern all numerics for this SDE system are

$$\begin{aligned} X_{t+\Delta t} - X_t &= \mu_x \Delta t + (\sigma_{xx}\zeta_X + \sigma_{xz}\zeta_Z)\sqrt{\Delta t} \\ Z_{t+\Delta t} - Z_t &= \mu_z \Delta t + (\sigma_{xz}\zeta_X + \sigma_{zz}\zeta_Z)\sqrt{\Delta t} \end{aligned} \tag{3.5}$$

with, again, ζ_X and ζ_Z composing a 2D standard Wiener process.

3.1. Boundary Conditions and Deposition Algorithm. The 2D SDE model consists of an ensemble of individual particle trajectories over time, where particles move freely in the fluid until encountering a boundary. The stochastic models in the previous section do not incorporate the influence of any boundary conditions. To supplement the SDE with boundary conditions, we have reflective boundary conditions following Erban and Chapman's algorithm for simple reflective boundary conditions [3]. Rather than the complex Robin boundary conditions proved in Leimkuhler et al. [9], we instead govern the moving boundary condition with flux by probability function (3.6). Particles that hit the wall, $X_t = 1$, may be deposited depending on the local concentration of particles. The concentration will be calculated as the number particles in a small area near the wall divided by that area. If concentration near the wall is above the threshold $C = 1$, our approximation is to take the probability that particles hitting the wall actually deposit as

$$P(C) = \begin{cases} 1 - e^{-k(C-1)} & C \geq 1, \\ 0 & C < 1. \end{cases} \tag{3.6}$$

This probability increases to 1 as C becomes large, and also includes the small possibility that particles do not deposit despite the concentration being over-saturated. After finding $P(C)$, we generate a uniform random number and determine whether it is above $P(C)$, depositing the particle if so.

A representative step $(X_t, Z_t) \longrightarrow (X_{t+\Delta t}, Z_{t+\Delta t})$ with conditions at all four boundaries is described by the algorithm in Algorithm 3.1 [3]. All coordinates are scaled to a fixed computational domain similar to the PDE model, so particles must stay in the domain $[0,1] \times [0,1]$. In the algorithm, a uniform random variable, called U, is compared against $P(C)$. If $U < P(C)$, the particle trajectory is terminated. If deposition occurs, the wall inches into the fluid and the radius decreases by a small amount δ, set to be around 0.1-1% the width of the pore [12]. Similar to how the volume scaling fraction γ in the PDE model accounts for reduction in particle size after deposition, δ is set to be a small particle size relative to the pore channel. As evaporation occurs, particles in the main fluid body are computationally scaled, but the pore channel radius is not. Thus, in response to the fluid level lowering,

Algorithm 3.1 Particle Trajectory $(X_t, Z_t) \longrightarrow (X_{t+\Delta t}, Z_{t+\Delta t})$

Given X_t, Z_t, t, and $C(X_t, Z_t, t)$, compute $(X_{t+\Delta t}, Z_{t+\Delta t})$ from Equation (3.5). Also, calculate probability $P(C_t)$ based on an average C_t according to the number of particles in a small neighborhood of the wall at height Z_t.

while $Z_{t+\Delta t} < 0$ or $Z_{t+\Delta t} > 1$ **do**
  if $Z_{t+\Delta t} < 0$ **then**
    Reflect: $Z_{t+\Delta t} = -Z_{t+\Delta t}$
  end if
  if $Z_{t+\Delta t} > 1$ **then**
    Reflect: $Z_{t+\Delta t} = 2 - Z_{t+\Delta t}$
  end if
end while
while $X_{t+\Delta t} < 0$ or $X_{t+\Delta t} > 1$ **do**
  if $X_{t+\Delta t} < 0$ **then**
    Reflect: $X_{t+\Delta t} = -X_{t+\Delta t}$
  end if
  if $X_{t+\Delta t} > 1$ **then**
    Calculate probability $P(C_t)$ from Equation (3.6) and generate a uniform random number U from (0,1)
    if $U < P(C_t)$ **then**
      Terminate particle trajectory and decrease pore radius by approximated particle size at height Z_t (deposition)
    else
      Reflect: $X_{t+\Delta t} = 2 - X_{t+\Delta t}$
    end if
  end if
end while
return $(X_{t+\Delta t}, Z_{t+\Delta t})$

the number of particles deposited on the walls is distributed according to a new partition of the radius in order to preserve mass. In Equation (3.6), the parameter k is a constant chosen to minimize mean-squared error (MSE) between the dry deposition patterns of the PDE and SDE model. To determine this constant, we found values for k across different initial conditions where the MSE is minimized, then the average, $k = 0.036$, is taken as the constant. While Leimkuhler et al. proposed a sophisticated stochastic approximation for Robin boundary conditions, Equation (3.6) will be shown in later sections to be a simpler, yet physically reasonable formulation for deposition. We recognize that the choice for (3.6) breaks the mathematical connection between the PDE and SDE boundary conditions, but also highlight that even with its simplicity it can capture the physical process of deposition and produce comparable deposition results.

4. 1D Asymptotic problem. Using the same nondimensionalized parameters from Table 2, we now let $\epsilon \to 0$, which implies $\boldsymbol{R}/\boldsymbol{H}$ will approach zero. Recalling that ω, appearing

in equations (2.8) and (2.9), is defined as $\frac{\lambda \boldsymbol{H}^2}{D\boldsymbol{R}}$, if the other dimensional values are held constant, ω will approach infinity. But introducing a new parameter ψ such that the relation $\lambda = \psi\epsilon$ holds with ψ held constant will prevent ω from producing singular limits. In Equation (2.13), by letting ϵ go to zero, perturbation expansions for both $\tilde{C}$ and $\tilde{R}$ to their second leading order terms with respect to ϵ^2 are $\tilde{C} = \tilde{C}_0 + \epsilon^2\tilde{C}_2 + O(\epsilon^4)$, $\tilde{R} = \tilde{R}_0 + \epsilon^2\tilde{R}_2 + O(\epsilon^4)$[1]. We group by powers of ϵ for the diffusion equation (Equation (2.13)) and each boundary condition (Equations (2.14)-(2.17)) at $O(\epsilon^0)$ and $O(\epsilon^2)$. Grouped by order, the $O(\epsilon^0)$ sub-problem can be written as

$$\tilde{C}_{0\tilde{x}\tilde{x}} = 0, \qquad \beta\tilde{C}_0 - \tilde{C}_{0\tilde{z}} = 0\Big|_{\tilde{z}=\tilde{H}}, \qquad \tilde{C}_{0\tilde{z}} = 0\Big|_{\tilde{z}=0}, \qquad \tilde{C}_{0\tilde{x}} = 0\Big|_{\tilde{x}=0,\tilde{R}_0}$$

In $O(\epsilon^0)$, $\tilde{C}_{0\tilde{x}\tilde{x}} = 0$ is the PDE representing the system, and $\beta\tilde{C}_0 - \tilde{C}_{0\tilde{z}} = 0$ represents the top boundary, $\tilde{C}_{0\tilde{z}} = 0$ represents the bottom boundary, and $\tilde{C}_{0\tilde{x}} = 0|_{\tilde{x}=0,\tilde{R}_0}$ represents the left and right boundaries. The $O(\epsilon^2)$ sub-problem is

$$\tilde{C}_{2\tilde{x}\tilde{x}} + \tilde{C}_{0\tilde{z}\tilde{z}} - \tilde{C}_{0\tilde{t}} = 0, \qquad \beta\tilde{C}_2 - \tilde{C}_{2\tilde{z}} = 0, \qquad -\tilde{C}_{2\tilde{x}} - \tilde{Q}(\tilde{C}_0)\omega - \tilde{C}_0\tilde{R}_{0\tilde{t}} + \tilde{C}_{0\tilde{z}}\tilde{R}_{0\tilde{z}} = 0,$$

$$\tilde{Q}(\tilde{C}_0)\omega\gamma + \tilde{R}_{0\tilde{t}} = 0.$$

Solving for $\tilde{C}_0$ by integration and using boundary conditions at the top and bottom reveal that $\tilde{C}_0$ is independent of $\tilde{x}$. Further substitution derives the following asymptotically reduced equation for the model:

$$-\tilde{Q}(\tilde{C}_0)\omega + \tilde{R}_0(\tilde{C}_{0\tilde{t}} - \tilde{C}_{0\tilde{z}\tilde{z}}) - \tilde{C}_0\tilde{R}_{0\tilde{z}} + \tilde{C}_{0\tilde{z}}\tilde{R}_{0\tilde{z}} = 0 \tag{4.1a}$$

$$\tilde{R}_{0\tilde{t}} = -\tilde{Q}(\tilde{C}_0)\omega\gamma \tag{4.1b}$$

The simplified equation with its boundary conditions is

$$(\tilde{C}\tilde{R})_{\tilde{t}} = (\tilde{C}_{\tilde{z}}\tilde{R})_{\tilde{z}} - \omega\tilde{Q}(\tilde{C}), \quad 0 \le \tilde{z} \le 1 - \beta\tilde{t} \tag{4.2a}$$

$$\left(\beta\tilde{C} - \tilde{C}_{\tilde{z}}\right)\Big|_{\tilde{z}=1-\beta\tilde{t}} = 0, \qquad \tilde{C}_{\tilde{z}}\Big|_{\tilde{z}=0} = 0 \tag{4.2b}$$

with initial conditions $\tilde{H}(0) = 1, \tilde{R}(\tilde{z},0) = 1, \tilde{C}(\tilde{z},0) = \rho$. With the asymptotic model, a change in variables was performed similar to that of the computational version of the main PDE as seen in Section 2.1.2.

5. Comparison of Results in Pore Channel Geometry. In this section, results from the 1D asymptotic model and the SDE model are compared against the 2D PDE problem. Pore evolution, concentration evolution, and deposition mass are analyzed as a means of determining if models corroborate each other.

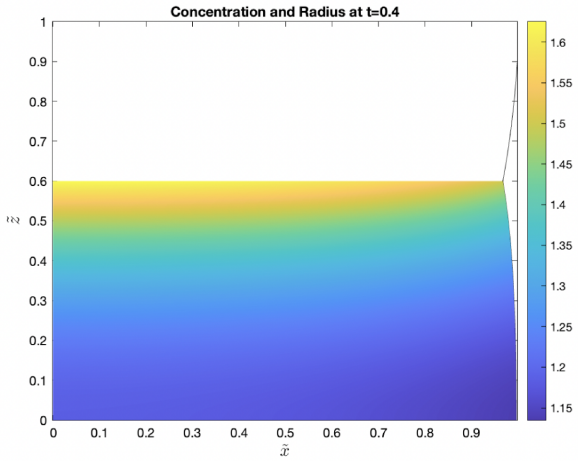

Figure 2: Concentration color plot and deposition pattern of the 2D PDE model at $t = 0.4$ with $\beta = 1$, $\omega = 0.6$, and $\boldsymbol{R} = 1$.

5.1. 2D PDE vs. 1D Asymptotic PDE. When the evaporating interface reaches a small height, the diminishing fluid volume and the increasing concentration of particles causes the model to enter a high concentration regime. Given that the model is dependent upon the assumption that particles have negligible volume, we no longer have confidence in the model when the concentration is no longer dilute. For all following results, simulations terminate at around heights 0.2 or 0.3, chosen from observation based on the combination of parameters in Table 1 as an estimation of the margin before the remaining fluid becomes too dense.

Figure 2 is a color plot of particle concentration when fluid height reaches 0.6 with $\beta = 1$. The figure is not displayed in the computational domain but in the non-dimensionalized physical $\tilde{x}$-$\tilde{z}$ plane. The radius profile is $\widetilde{R}_{full}(\tilde{z}, \tilde{t})$, but plotted with inverted axes to visually show how a deposition pattern may appear on a vertical pore channel wall. Greater adsorption occurs where local concentration far exceeds saturation ($\widetilde{C} > 1$), which we can see is most common near the evaporating surface, where the yellow color demonstrates highest particle concentration. Concentration is usually highest at the surface due to evaporation, and thus, regardless of different initial conditions, the pore radius at the surface will also be the narrowest at the current fluid height. Note that concentration is relatively uniform across $\tilde{x}$, besides slightly higher values towards the top center of the pore. Thus, averaging concentration values across $\tilde{x}$ will give a representative measurement of particle concentration at a given height $\tilde{x}$. In order to reduce the multi-variate function $\widetilde{C}$ shown in the color plot to 1D curves, we find

$$\langle \widetilde{C} \rangle := \frac{1}{\widetilde{R}} \int_0^{\widetilde{R}} \widetilde{C}(\tilde{x}, \tilde{z}, \tilde{t})\, d\tilde{x}. \tag{5.1}$$

Figure 3 is an example of a pore radius evolution plot and its corresponding concentration evolution plot. In Figure 3 (left), the horizontal arrow indicates the pore radius narrowing

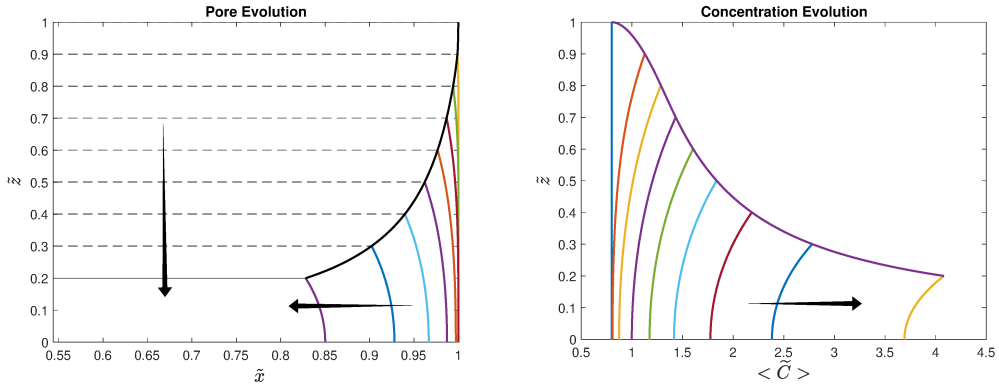

Figure 3: Evolution profiles produced by the 2D PDE model with $\boldsymbol{R} = 1$ and $\rho = 0.8$. Left: Pore Wall Evolution. Dotted lines demonstrate the decreasing fluid surface level at specific time points, and arrows indicate the direction of motion for top and right boundaries. Right: Concentration Evolution. The arrow shows direction of concentration evolution over time. Concentration profiles are determined from taking the mean concentration across $\tilde{x}$ for a given $\tilde{z}$.

inward over time due to deposition and the vertical arrow illustrates the fluid height decreasing during evaporation. Curves drawn at each 0.1 decrease in fluid height show particle deposition adding mass to the changing pore wall. $\widetilde{R}_{dry}(\tilde{z})$ lies above the fluid-air interface. At $\tilde{t} = 0.8$, the dry region above $\tilde{z} = 0.2$ (solid black line) is fixed and no longer experiences deposition, while anything below the black line is still submerged in fluid. We also plot the lowering interface with dashed black lines at each 0.1 increment. It is also noticeable in the figure that deposition does not begin immediately. Instead, deposition starts at around $\tilde{z} = 0.95$ due to the fluid starting under-saturated at $\rho = 0.8$.

The concentration evolution graph uses Equation (5.1) to find 1D concentration profiles, and plots them sideways to match the pore radius evolution graph. The initial profile in Figure 3 (right) is vertical line at ρ, with uniform concentration and no change in the system yet. Again at every 0.1 decrease in height, we plot the 1D curve at each time step, signified by different colors. The concentration is not uniform at each $\tilde{z} \neq 0$. The arrow further demonstrates to read the plot from left to right, since generally, the concentration increases as the height of the pore decreases. In both plots, we end the simulation at $\tilde{z} = 0.2$.

Deposition coefficient ω and evaporation rate β can be altered to investigate variations in the radius and concentration evolution. The radius evolution graph in Figure 4 reveals that a higher deposition rate coupled with a lower evaporation rate results in the radius rapidly shooting inward after a delayed initiation of deposition at around $\tilde{z} = 0.85$. For concentration, on the other hand, the low β high ω parameter combination leads to a drastic increase in fluid concentration towards the beginning but slows down dramatically after the fluid height reaches 0.7. Where there are high evaporation and low deposition rates instead, we see significantly less deposition and a concentration profile with larger concentration values in general. Faster

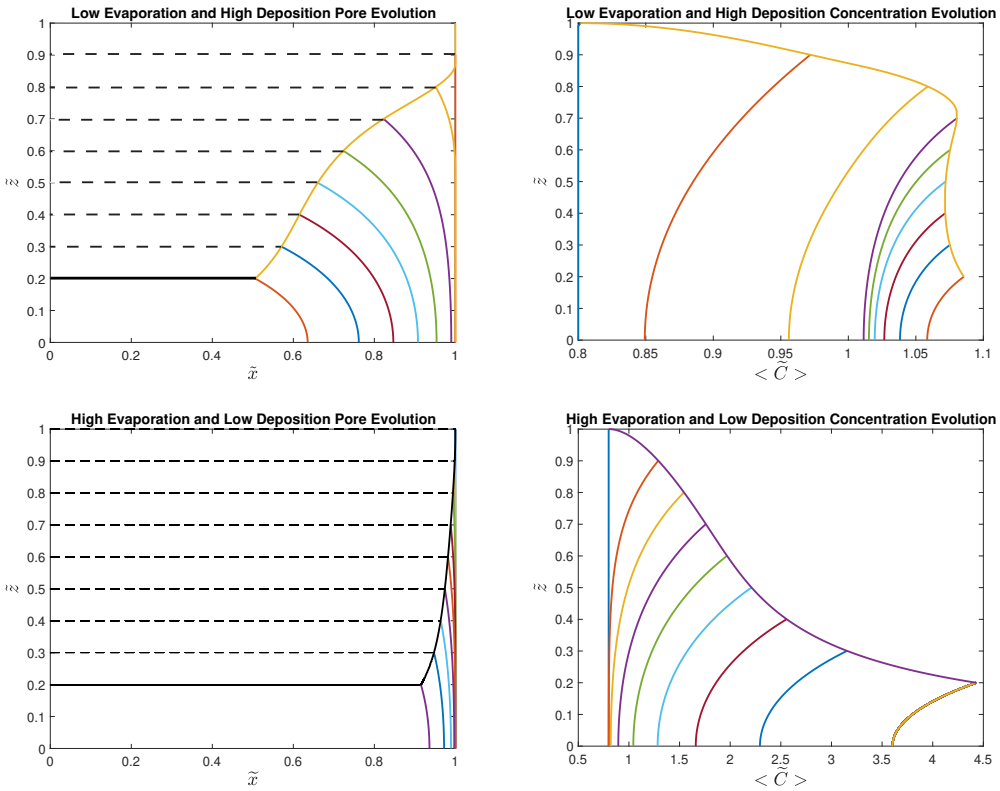

Figure 4: Pore radius and concentration evolution graphs for different combinations of evaporation (β) and deposition (ω) rates. Top row: low $\beta = 0.3$, high $\omega = 8$, $\rho = 0.8$, and $\gamma = 0.4$. Bottom row: high $\beta = 2$, low $\omega = 1$, $\rho = 0.8$, and $\gamma = 0.4$.

evaporation limits the time for particles to accumulate, while a lower deposition rate prevents deposition despite a high local concentration.

Figure 5 displays changes in $\widetilde{R}(\tilde{z}, \tilde{t})$ due to various values for $\boldsymbol{R}$, the initial pore width, in both the PDE 2D model and the asymptotically reduced model. The left graph displays the decrease of radius due to deposition from initial radius, that is $\widetilde{R}(\tilde{z}, 0.3) - \boldsymbol{R}$, with respect to $\tilde{z}$ at different initial radii. At $\epsilon = 0.1$, we only see one profile because the two models virtually overlap. The figure supports that as ϵ goes to zero, the results from the scaled 2D PDE model approach those of the asymptotic PDE model. An examination of deposited mass further validates this notion. The right graph in Figure 5 shows deposited mass, scaled by initial mass, in both the PDE asymptotic model (red) and the primary PDE 2D model (blue). In the range $\boldsymbol{R} \in [0.05, 0.1]$, there is a region where the two graphs coincide. Looking back at Figure 2, the general uniformity in concentration across $\tilde{x}$ also suggests that the 1D asymptotically reduced model is a good approximation of the 2D model. In fact, the simulation for Figure 2 was not performed with a small aspect ratio, where $\epsilon = 1$. Then, Figure 2 and Figure 5 both reveal that the asymptotic model is a reasonable approximation

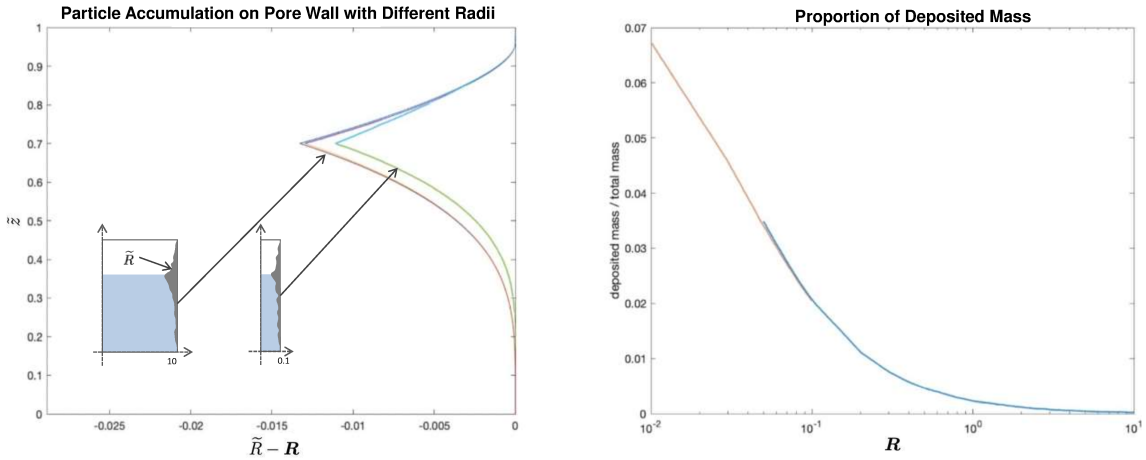

Figure 5: Left: $\widetilde{R}(\tilde{z}, 0.3) - \boldsymbol{R}$ with $\boldsymbol{R} = 10$, $\boldsymbol{R} = 1$, $\boldsymbol{R} = 0.1$ from left to right. Right: Mass of Deposited Particles/Total particles with respect to $\boldsymbol{R}$, with $\boldsymbol{R}$ on a logarithmic scale ($\boldsymbol{R} = 0.01$ to $\boldsymbol{R} = 0.1$ for asymptotic model (red); $\boldsymbol{R} = 0.05$ to $\boldsymbol{R} = 10$ for PDE 2D model (blue)).

of the 2D model, especially at relatively small aspect ratios.

5.2. Comparing PDE Model and SDE Model. Pore evolution in the SDE 2D model can also be graphed with both dry and wet sections shown together at different times, shown in Figure 6. As described in Section 3.1, we calculate the probability that particles exit the fluid by measuring local concentration at the wall. As fluid evaporates, particles become more packed and dense, resulting in higher probability for deposition and thus a gradual decrease in pore radius over time. The SDE model was also simulated in MATLAB. Comparing the SDE and PDE models on the same graph in Figure 6 shows that the dry portions of the deposited pattern agree, even more so at earlier times. Deposition patterns in the wet sections are dissimilar; however, we observe that when more fluid evaporates, the accumulated dry patterns still match up well. Differences in the PDE and SDE models appear to emerge towards the end of the simulation, but at that time, both models may be inaccurate from failure in holding the dilute assumption.

In both models, accumulation on the walls shows a concave-up pattern, with the peak height of accumulation at the fluid-air interface. Figure 7 (left) is a graph of the maximum accumulation $(1 - \widetilde{R})$ over time for one set of parameters, giving a percent error of 16.7% with the PDE model as the theoretical result. The right graph shows total dry mass over time, or total accumulation in $\widetilde{R}_{dry}(\tilde{z})$. There is close agreement between the two models, with a percent error of 5.4%.

We have observed general similarities between the SDE and PDE results, but we believe that differences appear from how boundary conditions are treated, particularly in the presence of flux or partial adsorption. Leimkuhler et al. [9] derived accurate stochastic Robin boundary

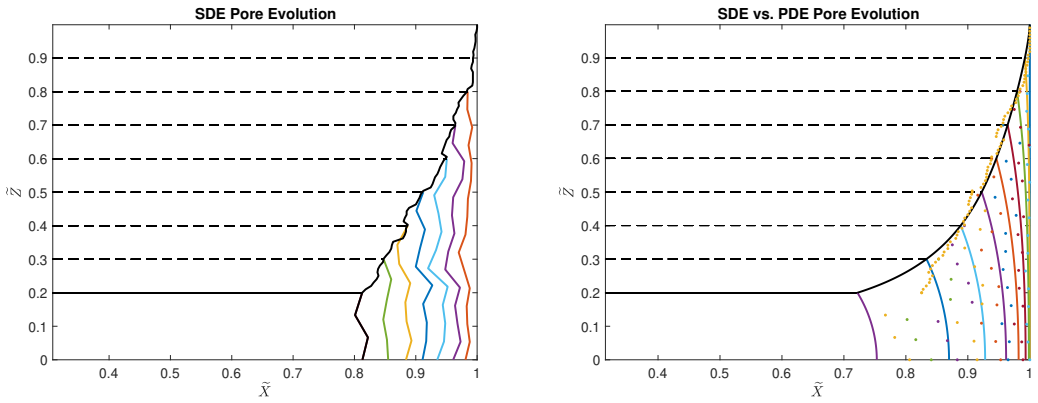

Figure 6: Left: SDE pore evolution at $t = 0.8$ and with $\rho = 1$, $D = 1$, and $E = 1$. Right: SDE (dotted) pore evolution compared with the PDE (solid) 2D model with $\rho = 1$ or $\boldsymbol{C_0} = 0.5$, $D = 1$, and $\beta = 1$.

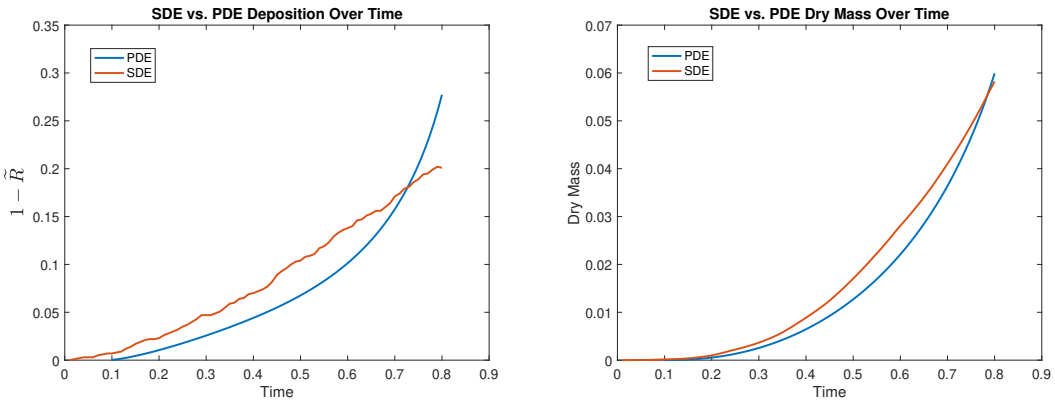

Figure 7: SDE and PDE $1 - \widetilde{R}$ (left) and dry mass (right) over time until $t = 0.8$, with $D = 1$, $\rho = 1$ or $\boldsymbol{C_0} = 0.5$, and $\beta = 1$.

conditions to approximate reflected stochastic differential equations, but to our knowledge, how to properly treat boundary conditions with flux, like Equation (2.21), has not been resolved. Our proposed probabilistic boundary condition in Algorithm 3.1 can at least produce comparable results for the dry portion of the deposition pattern in the dilute case.

6. Parameter Analysis in the 2D Model. This section explores how some of the parameters listed in Table 2 influence model attributes, such as the pore radius at a given height or the monotonicity of the concentration evolution. Deposition and evaporation are noted as opposite processes, where the former decreases particle concentration within the fluid and the latter increases it. The combined mechanism is analyzed at different degrees by varying their

rates.

6.1. Effects of Parameters. Highlighting specific characteristics of the model by performing sensitivity analyses on model parameters can provide critical information to improve industrial design. For example, the distinction between brine water and pure water (differences in concentration, evaporation rate, and concentration evolution) is crucial for designing anti-fouling/anti-salt accumulation solar evaporator technology for desalination [15].

For the following results, the system consistently evaporates to half height, or to 0.5 (with initial height of 1). First, we observe the relationship between pore radius at half height and parameters of interest. As expected, the radius decreases as the rate of deposition increases, though the negative relationship is not dramatic. We expect deposition and evaporation to work as opposing processes, where the former decreases particle concentration in the fluid and the latter increases concentration. Even when particles deposit from the fluid quickly, the rapid rate at which concentration is expected to change may be mitigated by a lower evaporation rate. Furthermore, the resulting radius at half height and evaporation rate have a positive relationship. Again, the rate at which the concentration changes is mitigated due to a higher evaporation rate and a relatively lower deposition rate, leading to a positive slope with small magnitude. In both cases, the concentration would fluctuate between being under and above saturation levels.

Other observations show that decreasing the initial concentration, ρ, results in pore radii that are significantly larger. The converse is also true: when ρ is higher, particle deposition is expected to occur earlier because ρ is initially closer to the saturation concentration. Additionally, an inverse relationship is observed between the pore radius and the volume scaling coefficient, γ. If γ is low, then there is less accumulation of particles inside of the pore. A higher value for γ implies that the pore would clog earlier. Thus, with increasing γ, the radius decreases continuously until it hits 0, since a radius cannot be negative.

In our investigation of these parameter properties, we are most interested how the system behaves when the evaporation rate β changes. It is not immediately obvious when exactly concentration reaches its saturation point. Figure 8 (left) displays results from a sensitivity analysis test of β and shows a curve is almost parabolic in a certain region. Therefore, there exists a point of stability at the critical point, where changes in β cause minimal changes in $\frac{dR}{d\beta}$. Labeling these points β^*, we seek to understand how stability changes when system parameters are altered. Relationships between β^* and both γ (volume scaling fraction) and ω (deposition rate) are found to be positive and monotonically increasing. This is because the system constantly seeks stability, correspondingly shifting the point of stability after changing some parameter. In other words, one can infer the influence of a balancing force; modifying γ and ω require corresponding changes in the point of stability.

6.2. Analyzing Monotonicity of Concentration. Again, due to assumptions, the radius must be monotonically decreasing; however, this is not the case for concentration. For example, Figure 8 (right) shows that in the heavily over-saturated regime, the concentration evolution is not monotonically increasing. This can be shown by the concentration increasing, then decreasing, and then increasing for parts of the profiles. Furthermore, this can be more easily identified by the fact that the concentration curves overlap, signifying a lack of mono-

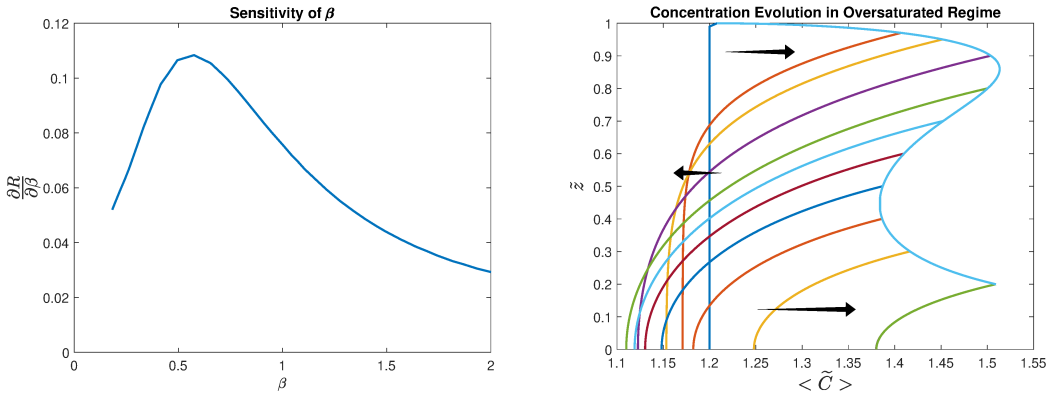

Figure 8: Top: $\partial R/\partial \beta$ (at height 0.5) against varying values of β. Bottom: Non-monotone concentration evolution in the over-saturated regime with $\beta = 1$, $\gamma = 0.4$, $\omega = 10$, and $\rho = 1.2$.

tonicity. To determine the criteria condition for non-monotone concentration evolution, the relationship between monotonicity of concentration evolution, ρ (scaled initial concentration), and γ is investigated. The result is demonstrated in the heat map Figure 9, where dark blue represents non-monotone concentration evolution and light blue represents monotone concentration evolution, γ is the horizontal axis and ρ is the vertical axis. Concentration appears to be non-monotone for large ρ. However, some points beyond C_{sat} (i.e. $\rho = 2$) contain initial conditions that still produce a monotone concentration evolution, possibly due to model assumptions creating close relations between local concentration and concentration in the rest of the fluid. Model assumptions also neglect that drift velocity (assumed to be zero) within the fluid which can contribute to imbalances in concentration in the fluid.

7. Droplet Model. Previously, we discussed models in which it was assumed that fluids reached from end of the wall to the other. However, in events in which this may not occur, droplets may potentially form. With this in mind, the two most prevalent scenarios for modeling a droplet is fixing either the radius of the droplet or the contact angle [17]. This paper will work with the former, and models the droplet surface with the parabolic equation

$$\widetilde{H}(\tilde{x},\tilde{t}) = \tilde{h}(\tilde{t})\left(1 - \left(\frac{\tilde{x}}{\boldsymbol{R}}\right)^2\right), \tag{7.1}$$

where $\tilde{h}(\tilde{t}) = 1 - \beta\tilde{t}$ is the maximum height and $\boldsymbol{R}$ is the fixed contact radius, set to 1. Again, only a half section of the 2D droplet is considered, drawn as a 2D parabola with an axis of symmetry at $\tilde{x} = 0$. In the PDE droplet model, the 2D nondimensionalized diffusion equation (2.13) is used to describe concentration within the droplet.

Discretizing the evolution of curved boundaries is more complex, so the top boundary of the droplet is approximated in a way that conserves particle mass. After evaporation, particles above the fluid-air interface are redistributed normal to the boundary, back into the

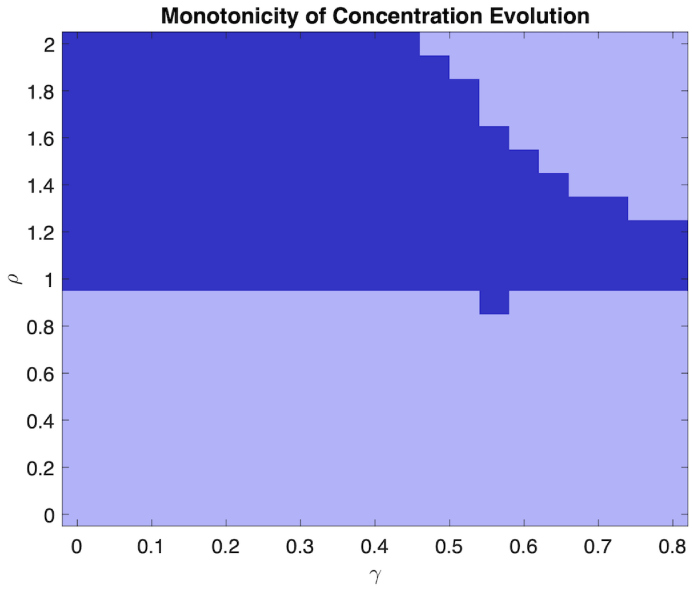

Figure 9: Regions of monotone vs. non-monotone concentration evolution according to variations in γ and ρ. Dark blue: non-monotone concentration evolution. Light blue: monotone concentration evolution.

computational domain. A fully absorbing boundary condition is chosen for the floor. Again, one-sided derivatives are implemented for the PDE boundary conditions.

The SDE algorithm is similar to the 2D model, where particles are reflected from the left and bottoms walls according to Algorithm 3.1; but, particles are reflected according to the normal vector at the boundary. Computational scaling for the droplet model in the SDE version of the droplet model similarly consists of bridging the scaled diffusion equation with the 2D FP equation, given by

$$\frac{\partial C}{\partial t} - \frac{\partial C}{\partial z}\frac{\partial H}{\partial t}\frac{z}{H} = \tag{7.2}$$

$$D\left(\frac{\partial^2 C}{\partial x^2} - \frac{\partial^2 C}{\partial x \partial z}\frac{\partial H}{\partial x}\frac{z}{H} + \left(\frac{\partial H}{\partial t}\right)^2 \frac{\partial^2 C}{\partial z^2}\left(\frac{z}{H}\right)^2 + 2\frac{\partial C}{\partial z}\left(\frac{\partial H}{\partial x}\right)^2 \frac{z}{H^2} - \frac{\partial C}{\partial z}\frac{\partial^2 H}{\partial x^2}\frac{z}{H} + \frac{\partial^2 C}{\partial z^2}\frac{1}{H^2}\right)$$

for $0 \leq z \leq 1$. Matching the velocity terms and the scaled diffusion coefficients, again the 2 by 2 matrix $\boldsymbol{\sigma}(\vec{x}, t)$ and the 2D vector $\vec{\mu}$ are solved for to write step equations just like (3.5).

7.1. Droplet Results. As previously mentioned, the PDE droplet has boundary conditions that match those of the SDE droplet in 1D. For the left boundary, one-sided Neumann boundaries are used in the PDE model and particles are reflected in the SDE model. At the floor, we implement a fully absorbing Dirichlet boundary for the PDE model and eliminate any trajectories that cross the floor for the SDE model. Unlike the 2D model, the droplet

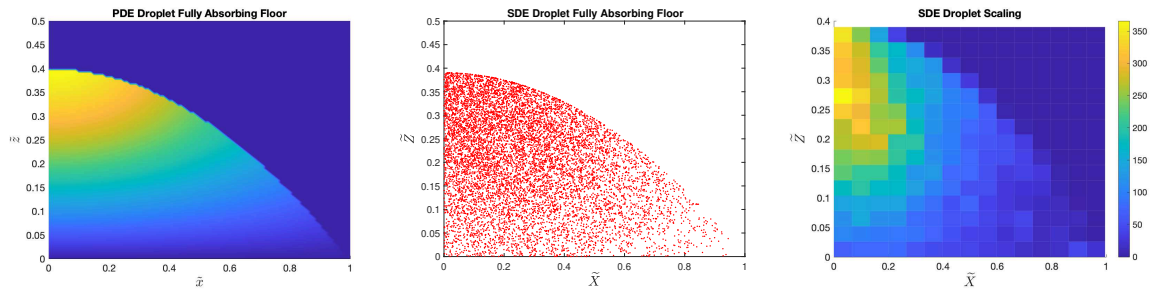

Figure 10: Particle distribution within a droplet with a fully absorbing floor. Parameters are $H_0 = 0.5, H_{end} = 0.4, D = 1, N = 40000$. Left: PDE with approximated boundary conditions. Middle: SDE with approximated boundary conditions. Right: SDE on a fixed computational domain with a partially absorbing floor.

contains a non-flat surface, thus each surface grid point is given an averaged corner boundary, with one-sided derivatives following the equation $DC_x + \frac{\partial H(x,t)}{\partial t} C = 0$. We compare the SDE and PDE model with a fully absorbing floor in Figure 10. The highest concentration of particles occurs at the top center of the droplet and disperses as they reach the floor, where they are 100% absorbed. However, due to the curved surface, the gradient is not uniform across the horizontal, leaving the corner with the least amount of particles. This pattern can be seen in both cases.

The sparsity of particles at the corner of the droplet may be attributed to 1) a lower number of particles reaching the corner or 2) more immediate absorption due to closer proximity to the floor. To determine which reason is more dominant, flux out of bottom of the droplet is observed for the PDE and SDE cases. For the PDE, flux is calculated at $z = 0$ using $-D\frac{\partial C}{\partial z}$, whereas its SDE counterpart simply counts the number of particle trajectories eliminated from the fluid after touching the floor. In Figure 11, both measurements of flux display similarly-shaped monotone decreasing curves, describing higher flux near the center of the droplet and less at the corner. If the sparsity of particles were attributed to faster adsorption (from a lower droplet height), the curves would be monotone increasing. Low flux at the corner indicates a lower number of particles reaching the droplet corner. For that reason, we expect no coffee ring effect [5]. This corroborates with assumptions because the model neglects surface tension properties needed to precipitate a ring of particles at the edge of the droplet.

The rightmost graph in Figure 10 is a heat map of particle concentration in a computationally scaled version of the SDE modeled droplet. Again, the Euler-Maruyama Method was used to approximate the SDEs found from Equation (7.2) for particles within the fluid body. A partially absorbing boundary is set at the floor, using the algorithm and probability function described in Section 3.1 and Equation (3.6). Similar patterns can be observed, where highest concentration exists at the peak of the droplet and the lowest concentration is found in the corner of the droplet. We also observed that accumulating floor deposition patterns indeed do not show a coffee ring effect, confirming conclusions made from graphing flux from

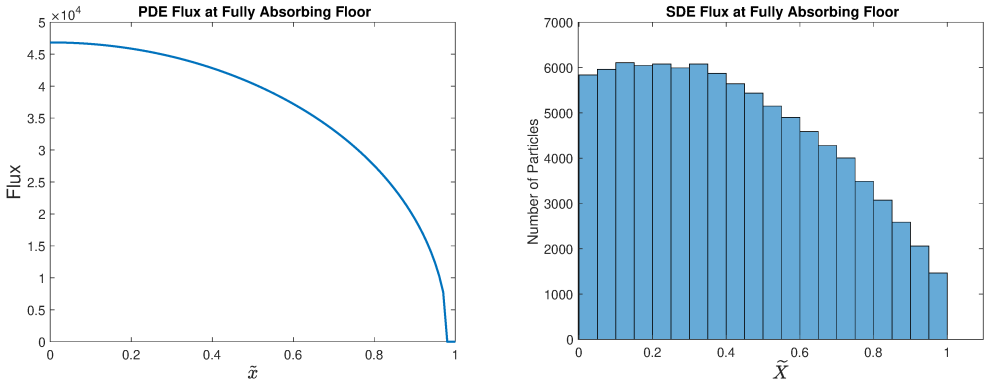

Figure 11: Flux distribution of a droplet with $H_0 = 0.5, H_{end} = 0.3, D = 1, n = 40000$ particles. Left: PDE, Right: SDE.

a fully absorbing floor.

8. Conclusion. Greater understanding of particle deposition in porous material resulting from the evaporation of impure fluids can help mitigate long-term contamination or clogging, optimizing membrane performance in various industrial applications, such as fabrics and other filtration systems. This study provides a comprehensive study and parameter analysis on particle behavior in pores with a 2D model that does not rely on a small aspect ratio. Visualizations of particle concentration give insight to particle distribution throughout a fluid, as well as pore radius and averaged concentration evolution patterns over time. Results show that particle deposition must accumulate given the assumption that deposition is irreversible, whereas concentration evolution is not necessarily monotonically increasing. The 2D PDE model produces steady results with initial radii between 0.05 to 10, where smaller radii begin exhibiting a small aspect ratio and give way to the asymptotically-reduced 2D PDE model. The asymptotic model is more computationally efficient for small initial radius (< 0.1).

Furthermore, the PDE model is compared with a stochastic interpretation that originates from leveraging connections between the 2D scaled diffusion equation and the 2D Fokker-Planck equation. A new algorithm for a partially absorbing SDE boundary is proposed. While there are some discrepancies in the behaviors of the PDE and SDE models, there are noticeable similarities between the models that allow for both a macro- and micro-scale understanding of physical phenomena in a fluid-filled pore channel. In particular, the SDE model is simpler when exploring different wall geometries, altering boundary conditions, and adding variation to particle-specific behaviors.

Since the PDE 2D model allows us to accommodate curved surfaces, the last part of the study investigates the behavior of a parabolic fluid-air interface through modeling the evaporation and deposition in a droplet. Concentration of particles and flux are visually comparable, exhibiting similar patterns. The SDE model, scaled or unscaled, is easier to manipulate and account for complex boundary conditions.

9. Future Work. Throughout this paper, we assume that the particle-laden fluids are originally dilute. In each simulation, we terminate the model before the evaporating surface reaches small $\hat{z}$, at which particles become too condensed [18, 13]. The model also assumes that particles are non-interacting and have negligible volume. This could be corrected using multi-phase mixture models that deal with higher particle density by incorporating non-constant diffusion. The nonlinear diffusion equation would then be

$$\frac{\partial \phi}{\partial t} = \nabla^2 (D(\phi)\phi).$$

Utilizing the nonlinear diffusion equation and PDE-related numerical methods, we can both validate existing assumptions with constant diffusion and dilute regimes, and generalize initial conditions to non-dilute solutions.

Additionally, we only consider a 2D quarter of the pore channel symmetric along the $\hat{x}$ and $\hat{z}$ axes. A more realistic geometry would be a 3D circular cylinder; the axi-symmetric version was done in [14]. Other physical considerations include curved interfaces due to surface tension, making the height $\widehat{H}(\hat{x}, \hat{t})$. Depending on the mixture and the material of the walls, the fluid may have inward or outward curved surfaces instead, forming menisci that evolves over time. In our model, local concentration also has a strong correlation with the concentration in the whole solution. As fluid evaporates and particle concentration increases, local concentration near the wall becomes greater than C_{sat} and yields deposition. We may also want to consider coupling the particle concentration to fluid dynamics for convection in the bulk. Ultimately, there is still much to be explored and expanded upon as we aim for a more comprehensive and thorough framework for fluid-filter phenomena.

Acknowledgments. This article would not have been possible without the exceptional support of our faculty supervisor, Dr. Thomas Witelski, and our graduate student supervisor, Yuqing Dai. We give credit to the study group report written during the 37th Annual Workshop on Mathematical Problems in Industry (MPI) in 2021, published in Mathematics in Industry Reports, for proposing the topics discussed in this paper and for laying the foundation for our research. We would also like to show our gratitude to Dr. Vasu Venkateshwaran from W. L. Gore & Associates, a material science company, who gave an industrial perspective to our work. An additional acknowledgement goes to Dr. Jonathan Mattingly for providing insight to stochastic boundary conditions. Lastly, we are also immensely grateful to Dr. Heekyoung Hahn and Dr. Lenhard Ng, co-directors for the DOmath program, for providing us with this opportunity. Some support for our project was provided by Dr. Witelski's grant, NSF DMS 2008255.

Appendix A. Derivation of Moving Boundary Condition. Here we derive the form of a prescribed-flux moving boundary condition (with prescribed normal flux $J(x,t)$); this is needed on two boundaries of our model. Let $C(x,z,t)$ be particle concentration defined on the region $0 < x < L$, $0 < z < G(x,t)$, and evolving according to the diffusion equation

$$C_t = D(C_{xx} + C_{zz}).$$

Let $F(x,z,t) := z - G(x,t)$ be the level set function defining the moving (top) boundary as $F = 0$. Assume there is no flux out through the left ($x = 0$), right ($x = L$), and bottom

($z = 0$) boundaries. Define $M(t) := \int_0^L \int_0^{G(x,t)} C(x,z,t)\, dzdx$ to be the total mass of particles in the domain at time t. Then, there is only flux through the top ($z = G$) boundary, and we have

$$\frac{dM}{dt} = -\int_{F=0} J(x,t)ds = -\int_0^L J(x,t)|\nabla F|dx \tag{A.1}$$

because the line integral can be represented as a single integral with respect to x, where the arclength ds is given by $|\nabla F|\, dx$. From another perspective, the rate of change in mass can also be expressed as

$$\frac{dM}{dt} = \int_0^L \left(\int_0^{G(x,t)} \frac{\partial C}{\partial t} dz + C(x, G(x,t), t) \frac{\partial G}{\partial t} \right) dx \tag{A.2}$$

by the Leibniz integral rule. Using the diffusion equation then gives

$$\frac{dM}{dt} = D \int_0^L \int_0^{G(x,t)} \nabla \cdot \nabla C dzdx + \int_0^L C(x, G(x,t), t) \frac{\partial G}{\partial t} dx. \tag{A.3}$$

The double integral can be written as a line integral using the 2D Divergence Theorem, resulting in

$$\frac{dM}{dt} = D \int_{\{F=0\}} \nabla C \cdot \frac{\nabla F}{|\nabla F|} ds - \int_0^L C \frac{\partial F}{\partial t} dx. \tag{A.4}$$

Again, rewriting the line integral gives

$$\frac{dM}{dt} = D \int_0^L \nabla C \cdot \nabla F dx - \int_0^L C \frac{\partial F}{\partial t} dx.$$

Equating Equation A.1 and Equation A.4 gives

$$D \nabla C \cdot \nabla F - C \frac{\partial F}{\partial t} = -|\nabla F| J$$

and finally, using $\nabla F = (-G_x, 1)$,

$$D C_x G_x - D C_z - C G_t = \sqrt{1 + G_x^2}\, J \tag{A.5}$$

which is then applied to the top and right boundaries in Section 2.1.

REFERENCES

[1] C. Breward, F. B. Planella, D. A. Edwards, K. Kiradjiev, A. Kovacs, S. L. Smith, D. Rumschitzki, P. Sanaei, Y. Sun, T. Witelski, and M. Zyskin, Evaporation from porous media, pore-level analysis. 36th MPI workshop report, 2020.

[2] M. K. Das, P. P. Mukherjee, and K. Muralidhar, Porous media applications: biological systems, in Modeling Transport Phenomena in Porous Media with Applications, Springer, 2018, pp. 123–154.

[3] R. Erban and S. J. Chapman, Stochastic modelling of reaction–diffusion processes, vol. 60, Cambridge University Press, 2020.
[4] D. Grolimund, M. Elimelech, and M. Borkovec, Aggregation and deposition kinetics of mobile colloidal particles in natural porous media, Colloids and Surfaces A: Physicochemical and Engineering Aspects, 191 (2001), pp. 179–188.
[5] E. He, D. Guo, and Z. Li, A widely applicable strategy for coffee-ring effect suppression and controllable deposition of nanoparticles utilizing ice drying, Advanced Materials Interfaces, 6 (2019), p. 1900446.
[6] J. Herzig, D. Leclerc, and P. L. Goff, Flow of suspensions through porous media—application to deep filtration, Industrial & Engineering Chemistry, 62 (1970), pp. 8–35.
[7] C. N. Kaplan and L. Mahadevan, Evaporation-driven ring and film deposition from colloidal droplets, Journal of Fluid Mechanics, 781 (2015), p. R2, https://doi.org/10.1017/jfm.2015.496.
[8] P. Lehmann, S. Assouline, and D. Or, Characteristic lengths affecting evaporative drying of porous media, Phys. Rev. E, 77 (2008), p. 056309, https://doi.org/10.1103/PhysRevE.77.056309.
[9] B. Leimkuhler, A. Sharma, and M. V. Tretyakov, Simplest random walk for approximating robin boundary value problems and ergodic limits of reflected diffusions, The Annals of Applied Probability, 33 (2023), pp. 1904–1960.
[10] T. Metzger and E. Tsotsas, Influence of pore size distribution on drying kinetics: A simple capillary model, Drying Technology, 23 (2005), pp. 1797–1809, https://doi.org/10.1080/07373930500209830.
[11] G. A. Pavliotis, Stochastic processes and applications: diffusion processes, the Fokker-Planck and Langevin equations, vol. 60, Springer, 2014.
[12] A. J. Pelley and N. Tufenkji, Effect of particle size and natural organic matter on the migration of nano-and microscale latex particles in saturated porous media, Journal of colloid and interface science, 321 (2008), pp. 74–83.
[13] A. F. Routh and W. B. Zimmerman, Distribution of particles during solvent evaporation from films, Chemical Engineering Science, 59 (2004), pp. 2961–2968.
[14] P. Sanaei, C. Breward, M. Ellis, S. Han, B. Holzer, H. Ji, H. El Kahza, S. L. Smith, S. Parsa, H. Reynolds, J. Troy, T. Witelski, N. Zhang, and M. Zyskin, Evaporation and deposition in porous media, Mathematics in Industry Reports, (2021).
[15] Y. Shi, C. Zhang, R. Li, S. Zhuo, Y. Jin, L. Shi, S. Hong, J. Chang, C. Ong, and P. Wang, Solar evaporator with controlled salt precipitation for zero liquid discharge desalination, Environmental science & technology, 52 (2018), pp. 11822–11830.
[16] S. F. Shimobayashi, M. Tsudome, and T. Kurimura, Suppression of the coffee-ring effect by sugar-assisted depinning of contact line, Scientific reports, 8 (2018), p. 17769.
[17] J. M. Stauber, S. K. Wilson, B. R. Duffy, and K. Sefiane, On the lifetimes of evaporating droplets, Journal of Fluid Mechanics, 744 (2014).
[18] T. Yoo, B. Chun, and H. W. Jung, Practical drying model for horizontal colloidal films in rapid evaporation processes, Drying Technology, 40 (2022), pp. 516–526.